J. Fluid Mech. (2022), *vol*. 938, A20, doi:10.1017/jfm.2022.174

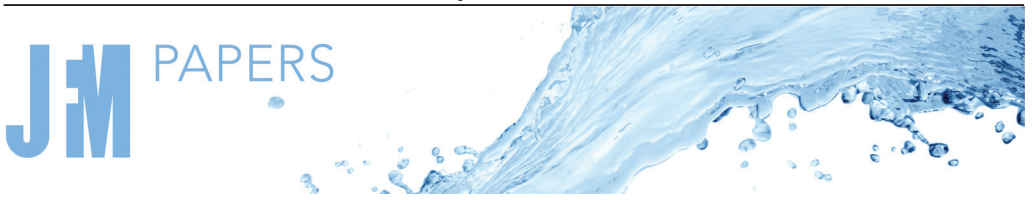

High-resolution fluid–particle interactions: a machine learning approach

Tsimur Davydzenka[1] **and Pejman Tahmasebi**[1],†

[1]College of Engineering and Applied Science, University of Wyoming, Laramie, WY 82071, USA

(Received 2 March 2021; revised 8 December 2021; accepted 22 February 2022)

Modelling of fluid–particle interactions is a major area of research in many fields of science and engineering. There are several techniques that allow modelling of such interactions, among which the coupling of computational fluid dynamics (CFD) and the discrete element method (DEM) is one of the most convenient solutions due to the balance between accuracy and computational costs. However, the accuracy of this method is largely dependent upon mesh size, where obtaining realistic results always comes with the necessity of using a small mesh and thereby increasing computational intensity. To compensate for the inaccuracies of using a large mesh in such modelling, and still take advantage of rapid computations, we extended the classical modelling by combining it with a machine learning model. We have conducted seven simulations where the first one is a numerical model with a fine mesh (i.e. ground truth) with a very high computational time and accuracy, the next three models are constructed on coarse meshes with considerably less accuracy and computational burden and the last three models are assisted by machine learning, where we can obtain large improvements in terms of observing fine-scale features yet based on a coarse mesh. The results of this study show that there is a great opportunity in machine learning towards improving classical fluid–particle modelling approaches by producing highly accurate models for large-scale systems in a reasonable time.

Key words: wet granular material, coastal engineering, river dynamics

1. Introduction

Problems of fluid–particle interactions are great in number, and they have constituted significant research topics in the areas of environmental engineering (control and management of such natural hazards as landslides and avalanches), chemical engineering (designing fluidized bed systems) and geo-systems, where fluid–solid interactions are a controlling factor on energy production. Depending on the scale and the complexity of the

† Email address for correspondence: ptahmase@uwyo.edu

problem, there have been many studies that have attempted to advance our understanding of these phenomena experimentally (Khan & Richardson 1989; Ling *et al.* 2012; Ramezani *et al.* 2018; Wagner *et al.* 2019). However, the common drawbacks of all experimental studies are that they are very difficult to accurately reproduce, and results are not as easily extractable. Furthermore, control of the boundary conditions is also difficult. Among the numerical approaches that allow modelling of fluid–particle interactions, the most significant ones are: lattice-Boltzmann method coupled with the discrete element method (DEM) (Lu & Hsiau 2008; Houlsby 2009; Rycroft, Orpe, & Kudrolli 2009; Hassanpour *et al.* 2011), smoothed particle hydrodynamics (Ji, Chen & Liu 2019; Xu, Dong & Ding 2019; Chen *et al.* 2020) and computational fluid dynamics (CFD-DEM) (Wu *et al.* 2010; Hager *et al.* 2011; Jayasundara *et al.* 2011; Chen *et al.* 2012; Tong *et al.* 2013; Zhao & Shan 2013*a*; Li, Zhao & Kwan 2020*b*).

The CFD-DEM method has been shown to be superior in terms of computational efficiency and is more numerically convenient than the methods listed above. This method, as an Euler—Lagrange method, uses CFD to solve the locally averaged Navier–Stokes equations to model fluid flow, and Newton's equation of motion for the system of particles through DEM, where CFD is continuum based, and DEM is a discrete-based method. The coupling between these methods is achieved by exchanging fluid–particle interaction forces, such as a viscous force, pressure gradient force and drag force (Tsuji, Kawaguchi & Tanaka 1993; Xu & Yu 1997; Xu *et al.* 2001; Zhu *et al.* 2007; O'Sullivan 2011). This method has been applied with great success to problems in a large number of applications, industries and engineering branches, including chemical and petroleum engineering, material processing, manufacturing and the mining industries, problems that involve large- and small-scale fluid–particle interactions (Zhu *et al.* 2008). More importantly, this approach has been successfully applied to problems related to geo-materials, such as underwater sandpile formation, flow under sheet pile walls, sinkholes and seepage flow in soils, and deformations in porous media (Suzuki *et al.* 2007; Chen, Drumm & Guiochon 2011; Zhao & Shan 2013*a*,*b*; Zhang & Tahmasebi 2019).

Nevertheless, the accuracy of this approach is largely dependent upon the size and number of mesh cells that are used in a given case. In an ideal scenario, regardless of the scale of the problem, one would use the maximum number and the smallest size of cells possible to capture all the fine-scale fluid features. However, this comes with a considerable computational trade-off. Increasing the number of cells boosts the number of computations that must be carried out for a particular domain. Therefore, depending on the problem, one must find compromises between fast, but inaccurate/accurate, and slow solutions. Sometimes it is possible to decrease the speed of the simulations by conducting mesh independence analysis to determine the largest size of mesh that can be used, without a significant loss of accuracy. But even then, improvements in CPU speeds are usually very insignificant. Furthermore, we always want to have the most accurate response and observe the fine-scale features produced by the fluid and solid whether we deal with small- or large-scale systems. Due to this computational obstacle, however, it has been generally accepted to use fine-mesh systems for small problems. Thus, observing such features for large problems is either not possible, or one must invest significant computational resources to accomplish it, which is often prohibitive. The comparison between coarse- and fine-scale modelling is shown in figure 1. As demonstrated, the coarse-scale modelling cannot show the fine-scale features and often suffices for a general, and crude, representation.

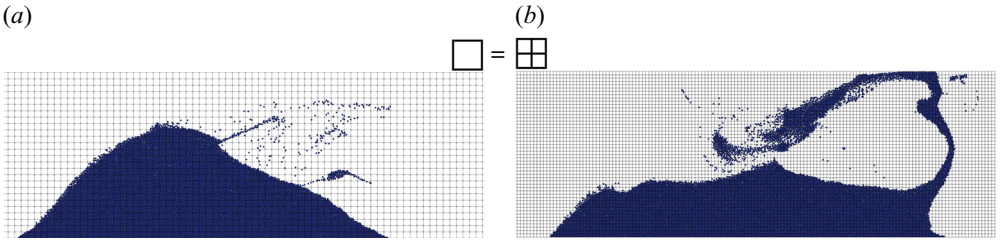

Figure 1. Comparison between (*a*) coarse-scale and (*b*) fine-scale modelling for the same time step.

With the recent developments in machine learning (ML) methods and their successful application to classical engineering problems, various advances have been made to accelerate numerical methods (Kachrimanis, Karamyan, & Malamataris 2003; Ariana, Vaferi, & Karimi 2015; Benvenuti, Kloss, & Pirker 2016; Chaurasia & Nikkam 2017; Liang *et al.* 2018*a*,*b*; Figueiredo *et al.* 2019; Brevis, Muga, & van der Zee 2020; Prieto 2020). This capacity has also been extended to problems related to fluid dynamics and granular flow (Radl & Sundaresan 2014; Kutz 2017; Wan & Sapsis 2018; Fukami, Fukagata & Taira 2019; Li *et al.* 2020*a*; Park & Choi 2020; Aghaei Jouybari *et al.* 2021) where its applications towards the former has been extensively reviewed (Brenner, Eldredge, & Freund 2019; Brunton, Noack, & Koumoutsakos 2020; Fukami, Fukagata, & Taira 2020*a*). For example, a ML approach was used for the estimation of gravitational solid flows (Garbaa *et al.* 2014). In a study conducted by Antony, Zhou & Wang (2006), a mechanistic neural network was applied to predict the micro-macroscopic behaviour of dense granular systems, subjected to quasi-static shearing. In another relevant study by Farizhandi, Zhao & Lau (2016), a ML method was developed towards modelling the change in the distribution of particles in fluidized beds. ML methods have also been applied to predict the permeability of loosely packed granular systems based on experimental and literature data (Mahdi & Holdich 2017). More importantly, ML has been applied in an Euler–Euler fluid–particle coupling problem to improve a filtered two-fluid model by estimating a drag correction for coarse-mesh simulations (Jiang *et al.* 2019). In their study, they were able to correct the inaccuracies that come with using a large-scale mesh when modelling gas–solid fluidized beds. All such developments have motivated us to tackle the complex problem of fluid–particle interactions using ML with the hope of improving such modelling by learning the phenomena that occur in fine-scale simulations and transferring them to coarse-scale models. Hence, as a result of investigating how ML can be applied to the problem of mesh dependence, one could improve the inherent inaccuracies associated with a coarse mesh when using classical coupling methods and retain the superior computational speed associated with large-mesh systems. In this paper, therefore, we do not aim to criticize the existing drag force models but to demonstrate how ML can potentially be used to enhance those models with lower accuracies for large simulation domains.

This paper, therefore, aims to improve the current multi-physics numerical framework for fluid–particle interactions and offer a more efficient alternative, which can make the application of such models more feasible for various problems in mining, chemical, geotechnical and energy resources, as well as to problems like prevention of debris flow and granular failure hazards. To do so, we will use ML due to its ability to work with large data and find complex relationships among them. In addition, the rationale behind using ML is that the drawbacks of the coupling methods, in particular the fluid

dynamics, could be mitigated by substituting some of the controlling computations with ML. To be more specific, we hypothesize that the drag force is the controlling factor in particle displacement, therefore we substitute the drag force calculations for large-scale problems with a ML model trained on fine-scale simulations to predict drag forces during run time based on fluid and particle velocities. Similar attempts have also been made to enhance the resolution of turbulent flows using an image-to-image regression, while we aim to improve the computations of fluid–particle interactions in a two-phase and dynamic system by substituting the drag force calculations in coarse-scale simulation via a pre-trained ML model on a fine-scale simulation (Fukami, Fukagata, & Taira 2020*b*; Kim *et al.* 2021). The final results of the coarse-scale coupling aided by ML have demonstrated significant improvements and greater similarity with the fine-scale (ground truth) modelling, compared with a classical coarse-scale simulation.

The remainder of this paper is organized as follows: in § 2 we discuss the methodology that we follow for conducting the numerical simulations for the fluid and solid, and we also briefly discuss the proposed ML method. In § 3 we outline the model set-up, its geometry and parameters that were used to conduct the simulations. Section 4 focuses on presenting the results obtained from three models, namely fine-scale, coarse-scale and coarse-scale ML-aided models. Finally, § 5 summarizes and concludes the paper.

2. Methodology

In this section, we will discuss the implemented modelling approaches to simulate fluid–solid interactions, the governing equations of which (i.e. CFD-DEM) can be found in many relevant studies (Xu & Yu 1997; Hager *et al.* 2011; Zhao & Shan 2013*a*,*b*; Ku, Li & Løvås 2015). First, we will elaborate on the major equations that are responsible for the particle–particle and particle–wall interactions. Then, we will discuss the methodology that stands behind the fluid component of the simulation. Third, we will provide the key equations that enable fluid–particle coupling and exchange of forces and momenta. Finally, we will discuss how ML is implemented to improve the capabilities of the utilized modelling and what network architecture was found to be most optimal in our simulations.

2.1. *Governing equations – particle system*

Most problems in fluid–solid modelling are approached by approximating inter-particle interactions, as in these cases such forces can be averaged (Hinch & Serayssol 1986; Yang *et al.* 2019) and treated as lubrication forces. However, in situations where particles are expected to undergo large displacements (i.e. granular column collapse), computing inter-particle interactions requires a greater precision (Topin *et al.* 2012). To this end, the DEM is fully capable of accomplishing this and is a promising methodology for our simulations.

DEM is a rapidly developing tool that has largely impacted the particle technology sector (Höhner, Wirtz & Scherer 2013; Vidyapati & Subramaniam 2013; Bertuola *et al.* 2016; Mandal & Khakhar 2016; Wan *et al.* 2018; Zhang *et al.* 2018*a*,*b*). Since its first formulation, there has been a great improvement in DEM in solving many micromechanical problems (Chen & Qiu 2012) such as soil consolidation (Cui, Chan, & Nouri 2017), erosion (Tang, Chan, & Zhu 2017), debris flow entrainment (Payne *et al.* 2008), granular flow mobility (Xu, Hu & Gao 2016; Ding & Xu 2018) and soil irregular vibration (Zhang *et al.* 2016; Zhang *et al.* 2018*a*,*b*).

In classical DEM, contact forces between objects are calculated by allowing a small overlap between the solid bodies (usually not larger than 5 % of the particle radius), where the forces are proportional to the amount of overlap. Thus, the choice of contact model becomes significant. In this study, since we are interested only in observing mechanical inter-particle behaviour, we adopt the Hertzian force model as it neglects cohesive forces between the particles (Hertz 1882). In our coupled system, the governing equations of particle motion are the classical DEM equations, extended by a force term $\boldsymbol{F}_i^f$, which accounts for the fluid–particle interactions

$$m_p \frac{\mathrm{d}\boldsymbol{v}_p}{\mathrm{d}t} = \sum_{N_{p,w}} \boldsymbol{F}_{p,w} + \boldsymbol{F}_p^f + m_p \boldsymbol{g}, \tag{2.1}$$

$$I_p \frac{\mathrm{d}\boldsymbol{\omega}_p}{\mathrm{d}t} = \sum_{N_{p,w}} \boldsymbol{M}_{p,w}, \tag{2.2}$$

where m_p is particle mass, $\boldsymbol{v}_p$ is the velocity of particles, $\boldsymbol{F}_{p,w}$ particle–particle or particle–wall force, $\boldsymbol{F}_p^f$ is the particle–fluid interaction force, $\boldsymbol{g}$ is gravitational acceleration, $\boldsymbol{\omega}_p$ is the angular velocity, I_p is the moment of inertia and $\boldsymbol{M}_{p,w}$ is the moment acting on particles, created either by other particles or walls. The particle–fluid interaction term $\boldsymbol{F}_p^f$ accounts for all fluid–solid interaction forces, namely the pressure gradient force $\boldsymbol{F}_{\nabla p}$, drag force $\boldsymbol{F}_d$, viscous force $\boldsymbol{F}_{\nabla\cdot\tau}$, virtual mass force $\boldsymbol{F}_{vm}$, Basset force $\boldsymbol{F}_B$, Saffman force $\boldsymbol{F}_{Saff}$ and Magnus force $\boldsymbol{F}_{Mag}$ (Crowe *et al.* 2011)

$$\boldsymbol{F}_p^f = \boldsymbol{F}_{\nabla p} + \boldsymbol{F}_d + \boldsymbol{F}_{\nabla\cdot\tau} + \boldsymbol{F}_{vm} + \boldsymbol{F}_B + \boldsymbol{F}_{Saff} + \boldsymbol{F}_{Mag}. \tag{2.3}$$

In most scenarios, the first three forces account for the majority of fluid–particle forces, and others may be neglected. Therefore, in our models we use

$$\boldsymbol{F}_p^f = \boldsymbol{F}_{\nabla p} + \boldsymbol{F}_d + \boldsymbol{F}_{\nabla\cdot\tau}. \tag{2.4}$$

As mentioned earlier, the Hertzian contact force model along with Coulomb's friction law are responsible for describing the interactions between particles (i.e. $\boldsymbol{F}_{p,w}$).

We use the Koch–Hill drag force (Koch & Hill 2001), given by

$$\boldsymbol{F}_d = \frac{V_p \beta}{\gamma_p}(\boldsymbol{u}_f - \boldsymbol{v}_p), \tag{2.5}$$

where V_p denotes particle volume and β is the interphase momentum exchange term, defined by

$$\beta = \frac{18\mu_f \gamma_f^2 \gamma_p}{d_p^2}\left(F_0(\gamma_p) + \frac{1}{2}F_3(\gamma_p) Re_p\right), \tag{2.6}$$

where γ_f is local porosity (volume fraction of fluid in a given cell), γ_p is the volume fraction of solid ($\gamma_f + \gamma_p = 1$) and

$$Re_p = \frac{\gamma_f \rho_f |\boldsymbol{u}_f - \boldsymbol{v}_p| d_p}{\mu_f}, \tag{2.7}$$

where ρ_f is the fluid density, $\boldsymbol{u}_f$ and $\boldsymbol{v}_p$ are fluid and particle velocities, respectively, d_p is particle diameter and μ_f is fluid viscosity.

Furthermore, functions F_0 and F_3 are given as

$$F_0(\gamma_p) = \begin{cases} \dfrac{1 + 3\sqrt{\dfrac{\gamma_p}{2}} + \dfrac{135}{2}\gamma_p \ln(\gamma_p) + 16.14\gamma_p}{1 + 0.681\gamma_p - 8.48\gamma_p^2 + 8.16\gamma_p^3} & \text{if } \gamma_p < 0.4 \\ \dfrac{10\gamma_p}{\gamma_f^3} & \text{if } \gamma_p \geq 0.4 \end{cases}, \tag{2.8}$$

$$F_3(\gamma_p) = 0.0673 + 0.212\gamma_p + \frac{0.0232}{\gamma_f^5}. \tag{2.9}$$

2.2. *Governing equations – fluid system*

Computational fluid dynamics (CFD) uses numerical analysis and data structures to analyse and solve problems that involve fluid flows and has been applied to a wide range of research and engineering problems. In this paper, CFD is coupled with DEM to calculate the drag, pressure gradient and viscous forces. To do so, the fluid domain is discretized into a set of cells, and the following governing equations are solved at each cell for locally averaged state variables, such as pressure, density and fluid velocity:

$$\frac{\partial}{\partial t}(\gamma_f \rho_f\ ) + \nabla \cdot (\gamma_f \rho_f) = 0, \tag{2.10}$$

$$\frac{\partial}{\partial t}(\gamma_f \rho_f \boldsymbol{u}_f) + \nabla \cdot (\gamma_f \rho_f \boldsymbol{u}_f \boldsymbol{u}_f) = -\gamma_f \nabla p - K_{pf}(\gamma_f \tau_f) + \nabla \cdot (\gamma_f \tau_f) + \gamma_f \rho_f \boldsymbol{g} + \boldsymbol{f}, \tag{2.11}$$

where γ_f is the void fraction (fluid content of a calculation cell), ρ_f is the fluid density, $\boldsymbol{u}_f$ is the fluid velocity, p is pressure, τ_f is the liquid stress tensor, $\boldsymbol{g}$ is the gravity vector and K_{pf} is the implicit particle–fluid momentum exchange term given by

$$K_{pf} = \frac{\gamma_f \cdot \left| \sum_p \boldsymbol{F}_d \right|}{V_{cell} \cdot |\boldsymbol{u}_f - \boldsymbol{v}_p|}. \tag{2.12}$$

In this approach, interaction forces for each particle are calculated first. To obtain K_{pf}, the forces of all particles in each fluid cell are summed.

2.3. *ML Assisted Modelling*

The model uses five variables as inputs, namely: (i) particle velocity in the X direction ($\boldsymbol{v}_{p,x}$), (ii) particle velocity in the Z direction ($\boldsymbol{v}_{p,z}$), (iii) fluid velocity in the X direction ($\boldsymbol{u}_{f,x}$), (iv) fluid velocity in the Z direction ($\boldsymbol{u}_{f,z}$), (v) void fraction. These variables are connected to two outputs which are the drag forces in the X and Z directions ($\boldsymbol{F}_{d,x}$, $\boldsymbol{F}_{d,z}$). The training set is obtained from the fine-scale modelling with a cell size of 4 cm, particle size of 0.1 cm and where the number of particles = 41 500; see figure 2. The fluid and particle properties of the training are identical to the ground truth modelling, as well as simulation control parameters such as time step and coupling interval. The training case was simulated for 7.5 s of free fall of the particle column. The architecture of the utilized ML is provided in figure 4. In particular, a multilayer-perceptron neural network model was

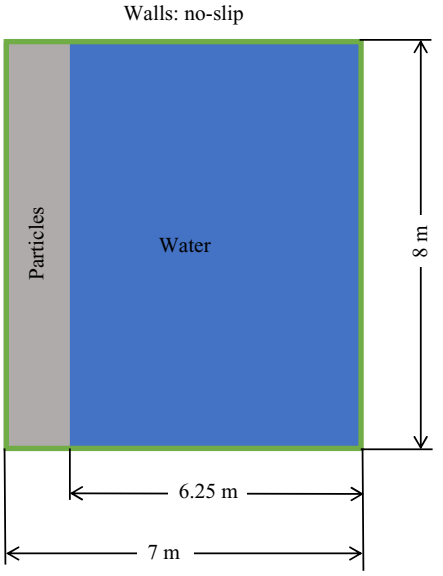

Figure 2. Numerical model set-up and the initial position of granular particles of the training dataset.

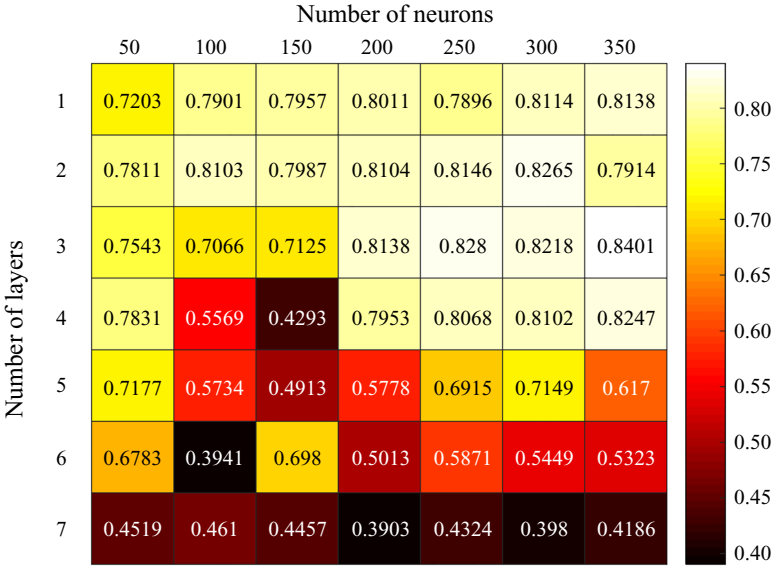

Figure 3. Sensitivity analysis of the effect of the number of layers and neurons on prediction accuracy, using the ELU activation function. The numbers in the matrix indicate R^2.

used for this task. In this paper, we optimized the architecture of the utilized network using the grid search method, which is a common method for parameter tuning (Liashchynskyi & Liashchynskyi 2019). This method automatically adjusts the hyperparameters by searching all possibilities and combinations such that the final estimations are optimum. Then, the final ML model is derived and used for all computations. An example of the effect of the number of layers and their neurons is provided in figure 3. In this study, a network with three hidden layers and [170 70 30] neurons is used, which resulted in a model with an

Activation Function	Equation	R^2
ReLU	$\varphi_{(x)} = \begin{cases} 0 & \text{if } x \leq 0 \\ x & \text{if } x > 0 \end{cases}$	0.8185
ELU	$\varphi_{(x)} = \begin{cases} \alpha(e^x - 1) & \text{if } x \leq 0 \\ x & \text{if } x > 0 \end{cases}$	0.8408
Sigmoid	$\varphi_{(x)} = 1/(1 + e^{-x})$	0.4113
Tanh	$\varphi_{(x)} = (e^x - e^{-x})/(e^x + e^{-x})$	0.7023
Softsign	$\varphi_{(x)} = x/(1 + \lvert x \rvert)$	0.7378
Softplus	$\varphi_{(x)} = \ln(1 + e^x)$	0.8332
SELU	$\varphi_{(x)} = \beta \begin{cases} \alpha(e^x - 1) & \text{if } x < 0 \\ x & \text{if } x \geq 0 \end{cases}$	0.8096
Loss Function	**Equation**	R^2
MSE	$L_{(y,y^p)} = \frac{\sum_{i=1}^{n} (y_i - y_i^p)^2}{n}$	0.8408
MAE	$L_{(y,y^p)} = \frac{\sum_{i=1}^{n} \lvert y_i - y_i^p \rvert}{n}$	0.3809
MSLE	$L_{(y,y^p)} = \frac{\sum_{i=1}^{n} (\log(y_i+1) - \log(y_i^p+1))^2}{n}$	0.1256
MAPE	$L_{(y,y^p)} = \frac{\sum_{i=1}^{n} \left\lvert \frac{y_i - y_i^p}{y_i} \right\rvert}{n}$	0.2449
Log-Cosh	$L_{(y,y^p)} = \sum_{i=1}^{n} \log(\cosh(y_i^p - y_i))$	0.7937
Training data size		R^2
1 000 000		0.8689
500 000		0.8642
250 000		0.8408
100 000		0.7881
50 000		0.7601
25 000		0.5913
10 000		0.2106

Table 1. Summary of sensitivity analysis for different parameters in our proposed ML network.

average accuracy coefficient of $R^2 = 0.8408$. Based on the further sensitivity analysis (table 1), we found that the exponential linear unit (ELU) activation function, mean squared error (MSE) loss function and training set that consists of 250 000 data points resulted in higher prediction accuracies. Model training specifications are summarized in table 2. In this paper, all R^2 values signify the average R^2 of $\boldsymbol{F}_{d,x}$ and $\boldsymbol{F}_{d,z}$, which is calculated using

$$R^2{}_{(y,\hat{y})} = 1 - \frac{\sum_{i=1}^{n} (y_i - \hat{y}_i)^2}{\sum_{i=1}^{n} (y_i - \bar{y})^2}, \tag{2.13}$$

where y_i is the true value of ith sample– $\hat{y}_i$ represents the predicted value for total n samples, and $\bar{y} = (1/n) \sum_{i=1}^{n} y_i$, i.e. the mean of the observed data.

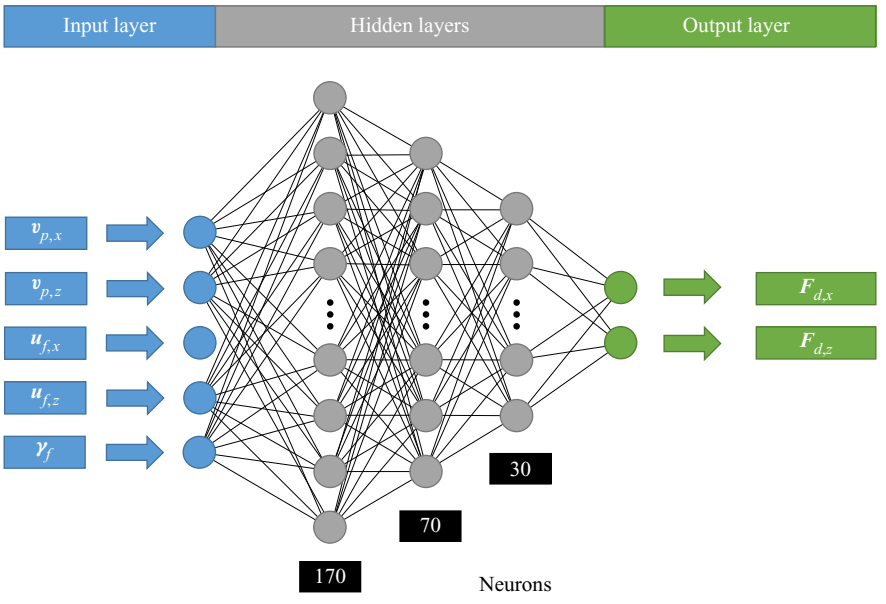

Figure 4. Our proposed ML architecture for estimating the drag force in the X and Z directions.

Parameter	Value	Parameter	Value
Number of hidden layers	3	Model optimizer	Adamax
Number of neurons	170–70–30	Learning rate	0.001
Number of epochs	2000	β_1	0.9
Training/Validation	85/15 %	β_2	0.999
Batch size	500	ε	1×10^{-7}
Training + Validation data size	250 000	Training CPU cost	1856 s

Table 2. Specifications used for training.

In this study, we assign an activation function to each node (neuron) of the network and determine whether the neuron should be activated, which depends on whether the input of that neuron is relevant to the prediction or not. To be more specific, we used the ELU activation function for all hidden layers. The output of this function is determined based on the following equation:

$$y = \begin{cases} \alpha(e^x - 1) & \text{if } x \leq 0 \\ x & \text{if } x > 0 \end{cases}, \tag{2.14}$$

where α is a coefficient. In most cases, this parameter is chosen to be between 0.1 and 0.3. The outputs of this activation function, therefore, range from slightly below zero (exponential relation in the case of $x < 0$) and $y = x$ (linear relation in the case of $x > 0$). To compare the effect of the activation function on the *a posteriori* results of the simulation we chose the three activation functions that performed best during the sensitivity analysis phase, namely ELU, Rectified Linear Unit (ReLU, table 1) and smooth approximation of ReLU (Softplus, table 1), and conducted three ML-assisted simulations on an 8 cm mesh. The results are shown in figure 5. Based on the visual analysis of the results, we concluded

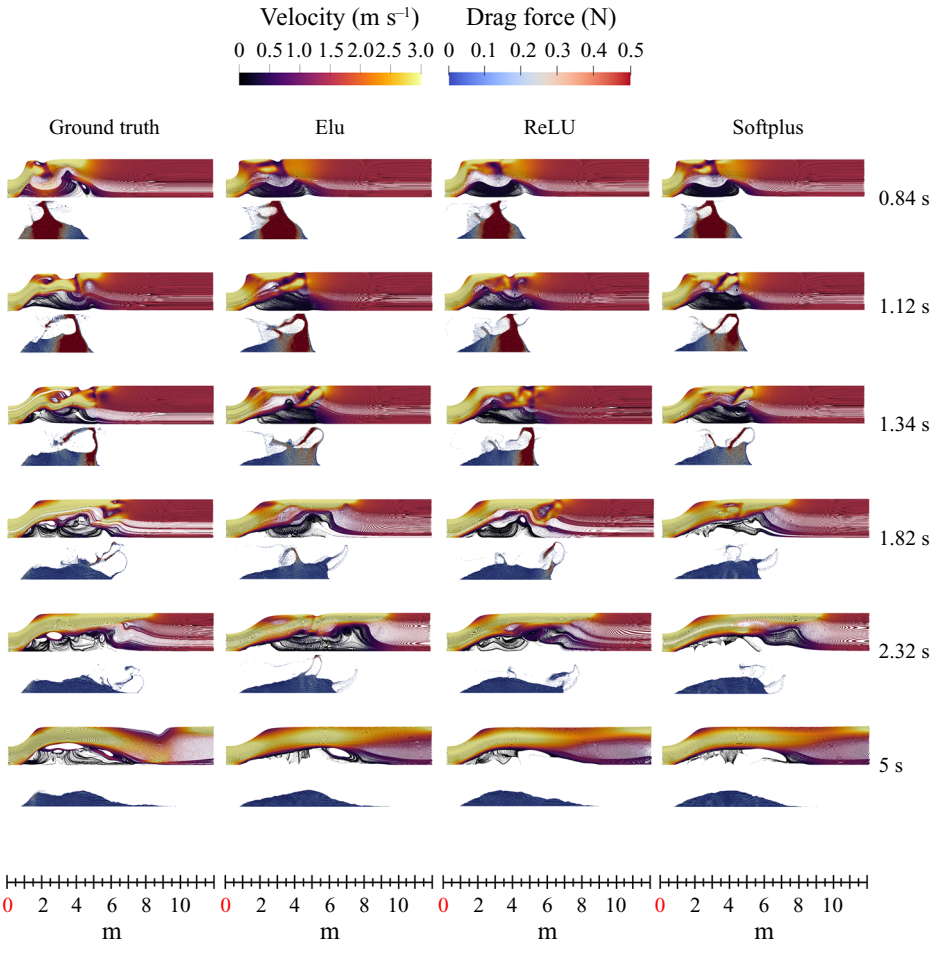

Figure 5. Runoff, velocity and drag force evolution for ground truth fine-scale (4 cm mesh) CFD-DEM, coarse-scale (8 cm mesh) ML-assisted modelling using the ELU activation function, coarse-scale (8 cm mesh) ML-assisted modelling using the ReLU activation function and coarse-scale (8 cm mesh) ML-assisted modelling using the Softplus activation function.

that ELU is optimal in terms of prediction accuracy during *a priori* training, and when used for *a posteriori* coarse-scale ML-assisted simulation. These results are also shown quantitatively in figure 6.

Another indispensable part of any neural network is a loss (cost) function. This function calculates the difference between the output of the algorithm and the true values, and it evaluates how well the model predicts the target values. The goal of the network is to minimize the output of the loss function and thereby increase the accuracy of predictions. For our network, we used the MSE loss function, which follows the expression below

$$\mathrm{MSE} = \frac{\sum_{i=1}^{n} (y_i - y_i^p)^2}{n}, \tag{2.15}$$

where y_i and y_i^p are true and predicted values, respectively, and n is the number of samples/data.

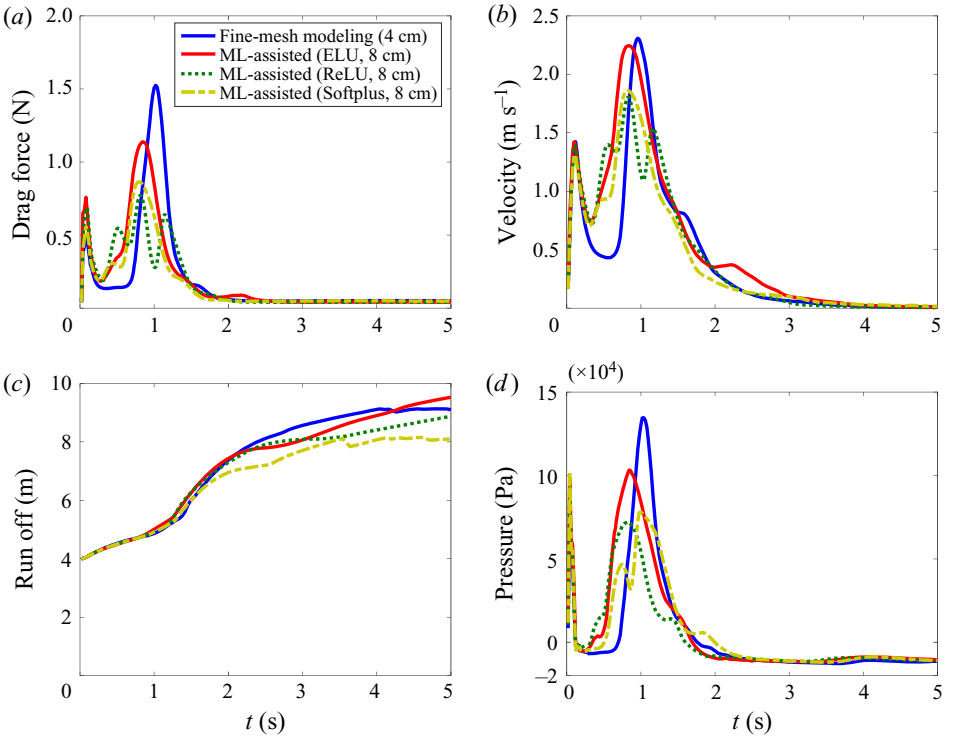

Figure 6. Quantitative comparison between the performances of several activation functions on the prediction capability of the proposed ML model.

To find the optimal weights and eventually minimize the loss function, we used backpropagation, which is a widely used algorithm in the training of ML. In this concept, the gradients of the activation functions in each successive neuron are tracked to optimize the weights and reduce the loss function. The gradients are then used by an optimization algorithm – AdaMax in our case – to update the model weights (Kingma & Ba 2015). It ultimately calculates to what degree the output values are affected by each individual weight of the model, by going back from the error function to a specific weight of a neuron.

The dataset was randomly split as follows: 85 % (212 500 data points) for training and 15 % (37 500 data points) for validation and 20 000 data points were used for testing. It should also be noted that only 2.3 % of the fine-scale data, which are generated from the training model (figure 2), are used for training. The reason for this was to make sure that the trained network is not biased toward the training and boundary conditions.

3. Model set-up

To demonstrate the performance of our proposed method, we used a two-dimensional polygonal pack with 20 000 spherical particles and water as an ambient fluid, where the properties of both phases are listed in table 3. For the coupling parameters between fluid and solid, we used a coupling interval of 50 (meaning that one CFD step is coupled with DEM after 50 DEM steps), and the drag force model was chosen to be the Koch—Hill model, as using this model we observed the greatest discrepancy between the fine and coarse cases. A schematic representation of the considered physical domain is shown in figure 7. As can be seen, this model is very different from the one we used for training the ML model (figure 2).

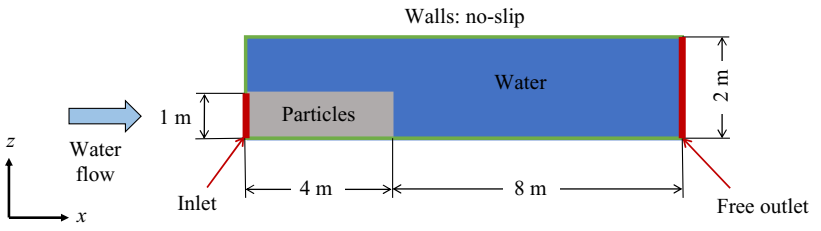

Figure 7. Numerical model set-up and the initial position of the utilized granular system for testing the proposed ML model.

Granular system	Size	20 000 particles, 0.01 mm in radius
	Particle density	5650 kg m^{-3}
Contact model parameters	Inter-particle and particle–wall friction coefficient	$\mu = 0.1$
	Young's modulus (Hertz model)	70 GPa
	Poisson's ratio	0.3
	Restitution coefficient	0.7
	Rolling friction	$\mu_r = 0.1$
Geometry	Height, Length, Width	2 m, 12 m, 0.04 m
Simulation control	Time step (DEM)	0.0002
	Time step (CFD)	0.01
	Coupling interval	50 (no. of DEM/CFD steps)
	Simulated real-time	5 s (25 000 steps in DEM)
Fluid properties	Viscosity	1×10^{-6} m^2 s^{-1}
	Density	1000 kg m^{-3}
	Cell size	Fine – 4 cm, Coarse - 8 cm, 16 cm, 32 cm.
	Number of cells	Fine (15 K), Coarse (3750, 900, 228)
	Drag force model	Koch–Hill
	Injection speed	3 m s^{-1}
***a priori* CPU time**	Training Case simulation	2080 s
	ML Training	1856 s
CPU time full simulation/Full case size/CFD part size	Fine CFD-DEM (4 cm)	1550 s /3.29 Gb/1.76 Gb
	Coarse CFD-DEM (8 cm)	800 s /2.29 Gb/0.75 Gb
	Coarse CFD-DEM (16 cm)	635 s /2.05 Gb/0.48 Gb
	Coarse CFD-DEM (32 cm)	627 s /1.98 Gb/0.42 Gb
	Coarse ML-CFD-DEM (8 cm)	865 s /2.29 Gb/0.75 Gb
	Coarse ML-CFD-DEM (16 cm)	776 s /2.05 Gb/0.48 Gb
	Coarse ML-CFD-DEM (32 cm)	695 s /1.98 Gb/0.42 Gb
CPU time per particle drag force calculation	CFD-DEM	4×10^{-7} s
	ML-CFD-DEM	1.75×10^{-5} s

Table 3. Model parameters used in the granular failure simulation.

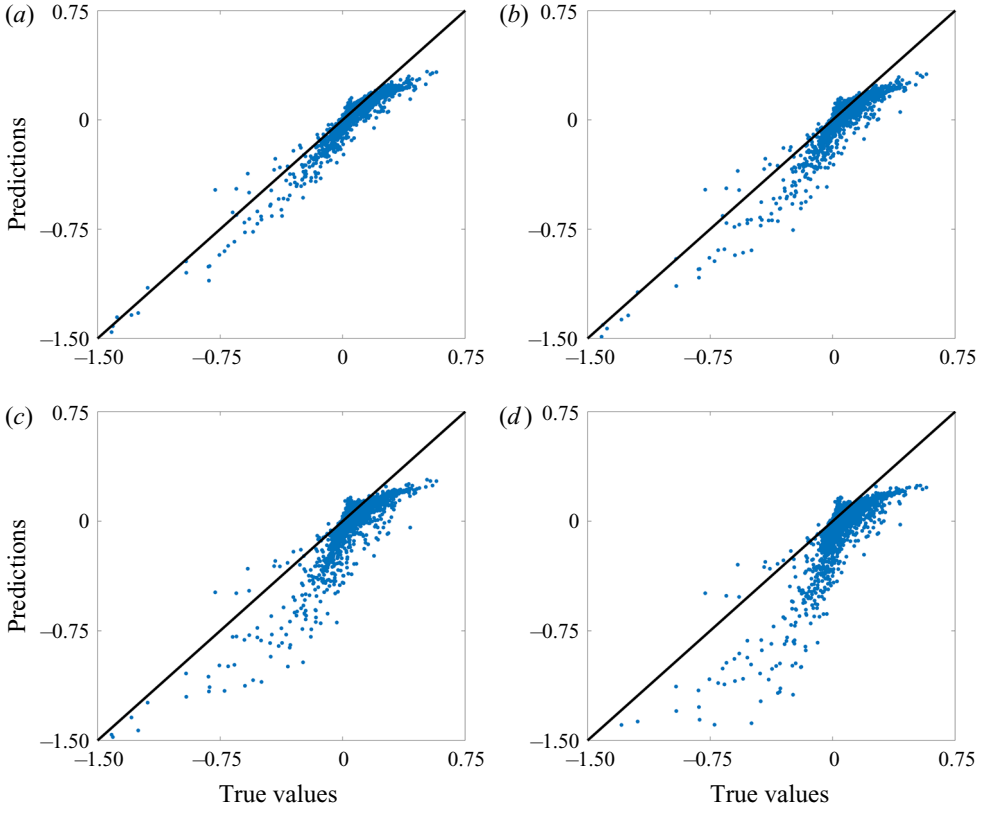

Figure 8. Parity plots between predicted and exact values of $\boldsymbol{F}_{d,x}$ and $\boldsymbol{F}_{d,z}$; (*a*) fine scale (4 cm mesh), (*b*) coarse scale (8 cm mesh), (*c*) coarse scale (16 cm mesh), and (*d*) coarse scale (32 cm mesh).

The simulations were carried out in parallel using 4 cores of an Intel i7-7700 CPU. The computational times of the simulations for fine (4 cm), coarse (8, 16, 32 cm) and coarse (8, 16, 32 cm) ML-assisted cases are presented in table 3. The trained network was converted to C++ and executed during run time to produce the desired drag force using the particle velocity, fluid velocity and void fraction as inputs. Figure 8 demonstrates the accuracy of the predictions using the ML-assisted model, where true values are the drag forces obtained from fine-scale modelling, (*a*) shows the model performance using identical input parameters as the fine-mesh simulation and (*b–d*) represent model performance using the averaged input values of the fluid velocity and void fraction according to the respective mesh resolution. Generally, the model demonstrates good predictions for the entire data range. It can be noted, however, that the accuracy of the predictions diminishes when the data approach negative values. This observation can be explained by the fact that the data in the training set are mostly positive, and the model did not have sufficient data (compared with the positive values) to be as accurate for negative values.

4. Results and discussion

In this study, seven simulations were performed on the geometry shown in figure 7, using the particle and fluid properties listed in table 3. To observe the differences between the fine and coarse models and then to be able to improve the coarse simulation, we conducted

an injection simulation in a granular pack, where the first case, representing fine-scale modelling, was performed using a 4 cm mesh and the second, third and fourth cases, representing the coarse-scale modelling, were performed using 8, 16 and 32 cm meshes, respectively. Similarly, the force computations were replaced with a ML model for the final drag force predictions in the later coarse models. The drag predictions (in the X and Z directions) are based on five inputs (particle and fluid velocities in the X and Z directions, and void fraction)

First, we visually discern substantial differences between the fine and coarse simulations in terms of particle runoff evolution and the final height of the granular system; see figure 9. Clearly, using a coarse mesh to solve the fluid–particle interactions results in a considerable loss in the ability of the utilized numerical simulation to demonstrate fine-scale features, and the coupling of the drag force between the fluid and solid becomes less accurate. This can be observed at all stages of the simulation and is most apparent during the first 1.5 s of injection, where the shock wave-like propagation of the granular system is observed in fine-scale modelling but is not present in the coarse modelling. We observe that, towards the first 40 % of the simulation time, the granular system in the coarse case has almost attained a form that is close to its final shape, without any considerable variation in height or increase in runoff, while the shape of the granular system in the fine mesh is very dynamic and the outer boundary of the granular system is gradually moving towards the outlet throughout the simulation. Furthermore, due to using a coarse mesh, the effect of the drag force on the particles becomes insignificant to the degree that water flow is reserved to a corner flow at the top of the domain, without affecting the particles underneath. This fact poses a problem, since, if a similar case was only performed on a coarse mesh and if it was related to a natural system, such as landslides or avalanches, then this modelling would present an overly optimistic result. The difference between the fine and coarse modelling in terms of the effects of the drag force can be visually confirmed in figures 9(*a*) and 9(*b*). As can be seen, the influence of the drag force on the movement of particles is much more significant in the case of fine-mesh modelling than it is in the coarse-mesh simulation. Therefore, it is clear at this point that the discrepancies between the fine and coarse models are substantial.

In figure 9(*c*), we present the results for ML-assisted modelling using a coarse mesh. From a visual examination of the evolution of the particle positions, we observe that the results of the proposed method using 8 and 16 cm mesh sizes are far closer to the fine-scale modelling, i.e. figure 9(*a*), than the corresponding coarse modelling, i.e. figure 9(*b*), even though we are still using a coarse mesh to conduct this simulation. We note that, at all stages of the simulation, the proposed ML-assisted modelling using the two mesh sizes mentioned above is much more similar to the fine case, indicating that the inherent issue of the loss in the accuracy associated with using a coarse mesh has been greatly improved. A simple visual comparison shows that the shape of the granular system at all stages of the simulation resembles the fine case. Furthermore, we observe that the height and run-off distance, in all ML-assisted cases, are dynamic, in contrast to the original coarse cases. Moreover, the distribution of the drag forces which are shown in figure 9 demonstrates that, although coarse mesh is used, the coupling between the fluid flow and particles is far superior in the ML-assisted case than in regular coarse-scale modelling. Figure 10 further demonstrates the ability of the proposed ML-assisted modelling to compensate for inaccuracies when using a coarse mesh. Here, one can observe that, proportionally to the drag force distribution, velocities of individual particles in the case of fine-scale modelling

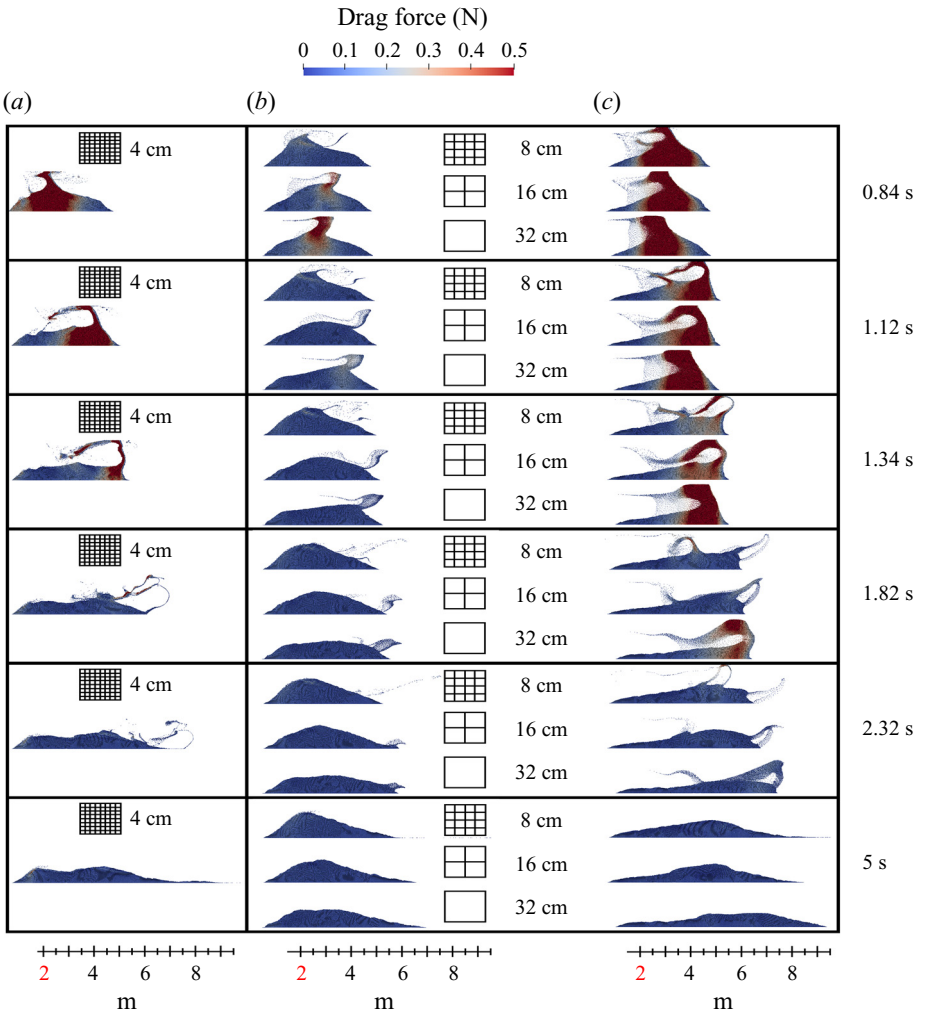

Figure 9. Runoff and drag force evolution for (*a*) ground truth fine-scale (4 cm mesh) CFD-DEM, (*b*) three coarse-scale CFD-DEM (8, 16, 32 cm meshes) and (*c*) coarse-scale (8, 16, 32 cm mesh) ML-assisted modelling.

and the proposed ML-assisted simulation (more so in the 8 and 16 cm cases) are largely similar and reside on the same scale at all stages of injection. Whereas the original coarse modelling demonstrates a comparative lack of particle movement.

The differences in the velocities in the system can be further observed in the evolution of the fluid velocity presented in figure 11. Here, we note that, as opposed to the fine mesh and ML-assisted modelling, the coarse-mesh modelling demonstrates a comparative lack of turbulent flow and vorticity in the system. The flow in the coarse-mesh modelling becomes relatively stable at the early stages of the simulation and the presence of the solid exerts only a superficial influence on the flow, compared with the original fine-scale case and the corresponding ML-assisted coarse cases. We also observe that, towards the fifth second of the simulation, the distribution of fluid velocities in the case of coarse-mesh modelling demonstrates a trend towards a sharp transition from smaller to larger velocities. This trend is also confirmed quantitatively in figure 15.

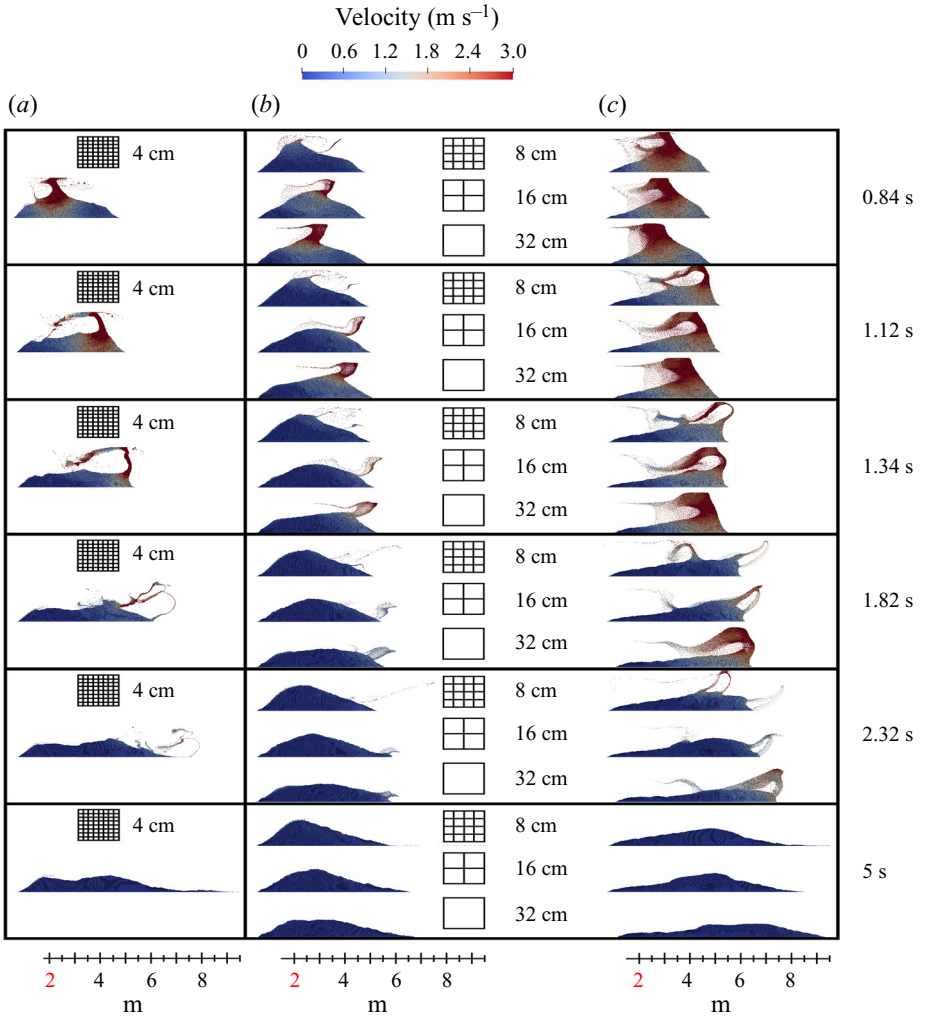

Figure 10. Runoff and particle velocity evolution for (*a*) ground truth fine-scale (4 cm mesh) CFD-DEM, (*b*) three coarse-scale CFD-DEM (8, 16, 32 cm meshes) and (*c*) coarse-scale (8, 16, 32 cm meshes) ML-assisted modelling.

In order to quantitatively compare the results for all three cases, we plotted several important and quantifiable parameters, which will assist us in conducting a more rigorous and detailed comparison. To be able to have a general understanding of the distribution of data in the domain, the average behaviours are compared. Furthermore, in some cases, and if necessary, more information is also provided. First, as the most important parameter in our methodology, the drag force data are presented in figure 12(*a*). The results suggest that the drag force data in the first two ML-assisted modelling cases (using 8 and 16 cm mesh sizes) are significantly closer to the ground truth case (fine-mesh modelling) than the corresponding coarse-mesh cases, and the last ML-assisted case (32 cm mesh) can also be considered an improvement as compared with the corresponding CFD-DEM case, but to a lesser degree. The proposed ML-assisted cases reflect the major spike in drag forces that are observed around first second of the simulation. Additionally, in order to confirm

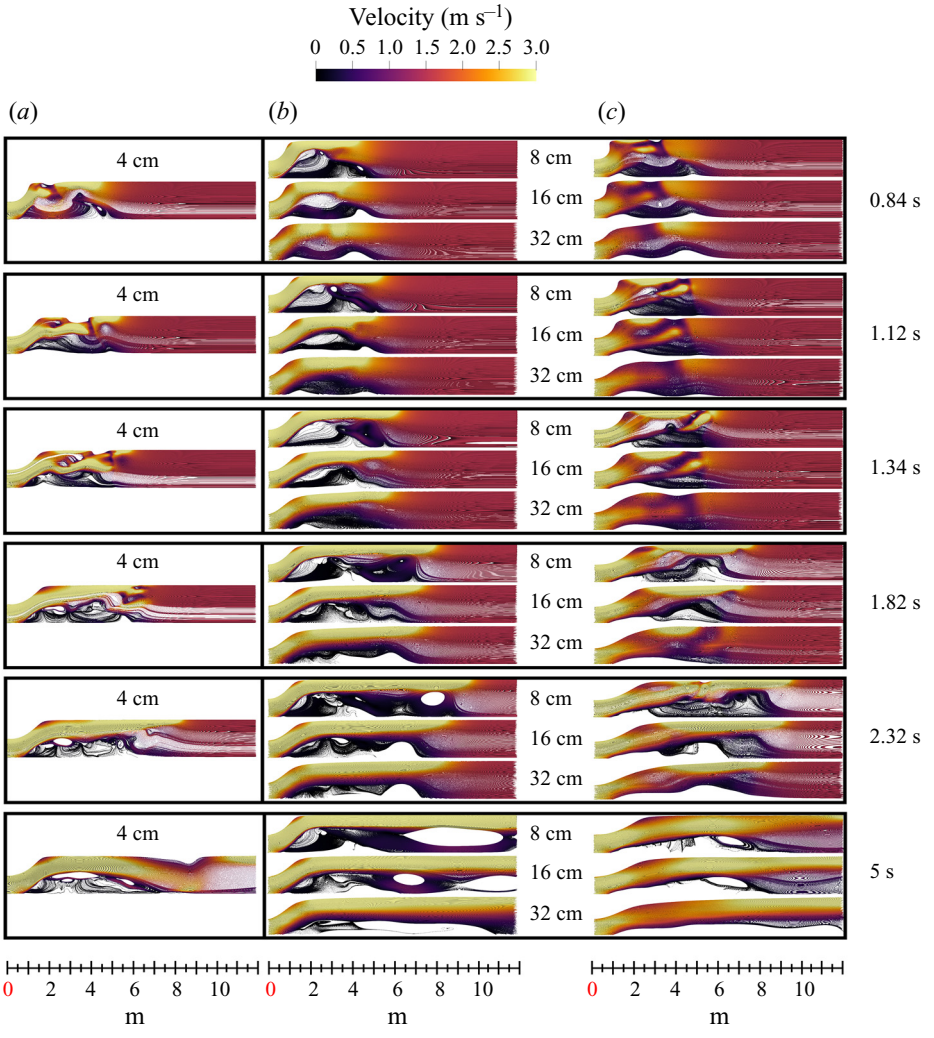

Figure 11. Fluid velocity evolution for (*a*) ground truth fine-scale (4 cm mesh) CFD-DEM, (*b*) three coarse-scale CFD-DEM (8, 16, 32 cm meshes) and (*c*) coarse-scale (8, 16, 32 cm meshes) ML-assisted modelling.

that the results of the simulations can be reliably reproduced by conducting identical *a priori* ML training and using the produced network for future simulations, we conducted three identical trainings (each time with a different seed number) which are then used on the same coarse-scale ML-assisted simulations (8 cm mesh). This analysis allows one to observe how ML models with different initializations can affect the responses. These results are presented in figure 12. Here, the upper and lower bounds of the cloud region indicate the maximum and minimum values obtained from coarse-scale ML-assisted simulation for a particular time step.

Furthermore, to see how our ML-assisted modelling performs compared with other well-established methodologies for calculating the drag force, we selected two additional methods, namely those of Di Felice (1994) and Gidaspow (1994), and performed identical CFD-DEM flow simulations using an 8 cm mesh. A quantitative comparison of the average

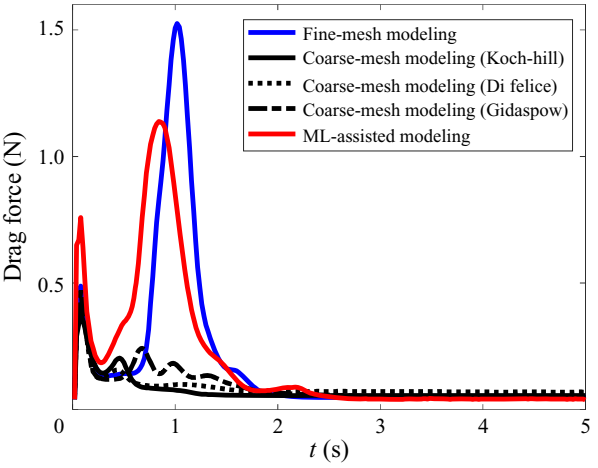

Figure 12. Comparison of average drag force evolution using fine (4 cm) mesh CFD-DEM; coarse (8 cm) mesh CFD-DEM using three most common models for calculating drag force, i.e. Koch–Hill, Di Felice, Gidaspow; and ML-assisted coarse (8 cm) CFD-DEM modelling.

drag force evolution is provided in figure 12. The individual drag force evolution curves suggest that the two additional classical drag force models perform very similarly to the Koch–Hill model, and demonstrate similarly poor performance on the coarse grid, compared with the ML-assisted modelling.

Another observation that we consider is that the spike in the case of the proposed ML-assisted modelling (for all mesh sizes, but less noticeably for 32 cm) comes 0.1–0.2 s earlier than in the ground truth case. This can also be confirmed by visual examination of the shape evolution snapshots in figures 9 and 10, where the top of the granular wave at the upper part of the domain in the case of ML-assisted modelling is moving ahead of the one shown in the ground truth case. Next, the particle velocities are shown in figure 13(*b*). Here, the similarity of the ML-assisted modelling to the fine-scale ground truth is even more apparent. More importantly, even at the 16 cm mesh size, where a significant discrepancy between the fine and coarse scales is expected, the ML-assisted modelling results are substantially closer to the ground truth than the corresponding coarse CFD-DEM, and the 32 cm ML-assisted case demonstrates a spike on a similar scale, however, its overall shape is less comparable to the original fine-scale CFD-DEM modelling. The third set of comparisons includes particle–particle and particle–wall collision forces; see figure 13(*c*). Here, the largest spikes (around 1 s) correspond to the moment when the particles hit the upper wall of the domain. The average values of the forces around 1 s quantitatively demonstrate that the collision forces in the cases of coarse-scale modelling are very insignificant, compared with the ground truth and the ML-assisted (8 and 16 cm) modelling, which is also evident visually in the snapshots shown in figures 9 and 10. The ML-assisted (32 cm) case, however, demonstrates no improvement in terms of collision force evolution. Next, the evolution of kinetic energy in the pack is shown in figure 13(*d*).

One of the most important quantifiable physical properties that we present in this study is the comparison of runoff and height evolution between all three cases; see figure 14. Here, we can confirm the previous visual observations regarding the differences between the fine- and coarse-scale modelling, and the similarities of fine-scale and

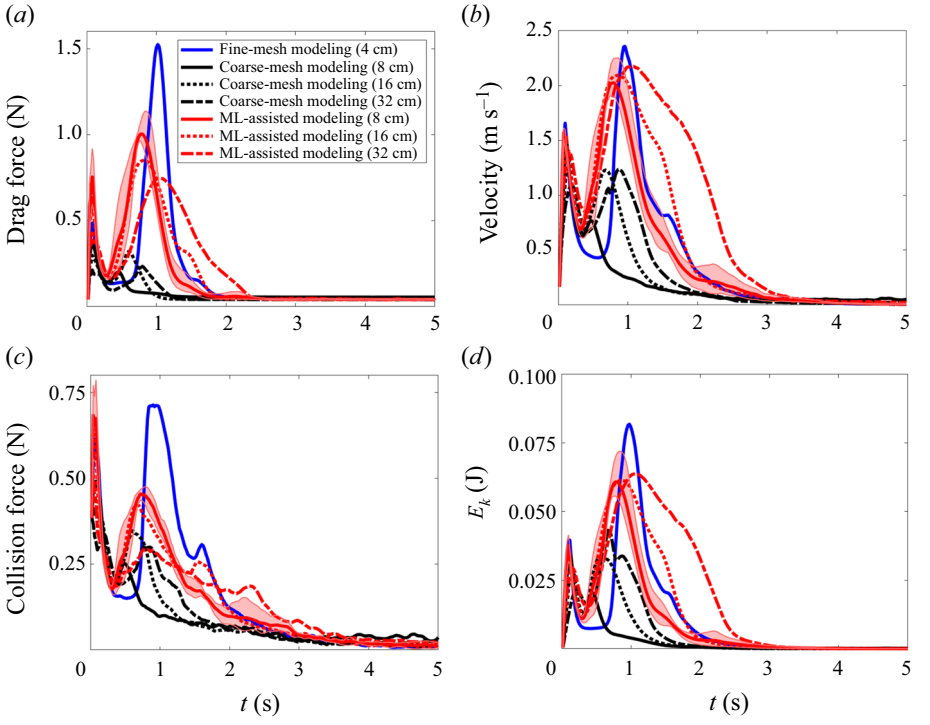

Figure 13. Uncertainty quantification of the effect of different initializations on the proposed ML model for predicting (*a*) drag force, (*b*) particle velocity, (*c*) collision force and (*d*) kinetic energy evolution of the granular system. The pink colour indicates fluctuations of the ML-assisted modelling (8 cm), where the solid red curve indicates the average value based on the conducted simulations.

ML-assisted simulations. The final run-off distance at the fifth second of the simulation for the ground truth CFD-DEM case (4 cm mesh) was 9.1 m, 5.9, 6.5, 6.9 m for the coarse-scale (8, 16, 32 mesh sizes) CFD-DEM and 9.5, 8.5, 9.4 m for the ML-assisted (8, 16, 32 mesh sizes) cases, respectively. In terms of the final height of the granular system, the values are 0.856 m (ground truth), 1.353, 1.151, 0.903 m (8, 16, 32 mesh sizes CFD-DEM) and 0.876, 0.94, 0.7 m (8, 16, 32 mesh sizes ML assisted). We also confirm that the height and run-off distance of the coarse-scale case undergo almost no changes after the first 2 s of the simulation, which is observed visually in figures 9 and 10 (except for height evolution of 8 cm mesh CFD-DEM modelling).

Another metric that we have included in this paper is the fluid pressure evolution; see figure 15. Compared with the coarse-scale simulation, the pressure values of the ML-assisted modelling are much closer to the fine-scale modelling, than in the original coarse-scale case. All ML-assisted cases are characterized by a major spike, similar to the ones found in other evolution plots (e.g. drag force, particle velocity, etc.). As expected, the overall resemblance to the fine scale diminishes with the increase in mesh size, where using 32 cm mesh resulted in a considerably less similar curve shape.

We also have compared the fluid velocity for all cases and the results are shown in figure 16. Here, the average values in all three cases are relatively similar. However, the median values suggest that the transition between the values of fluid velocity is much sharper in the case of coarse-scale CFD-DEM (8 cm mesh size) modelling. All these visual and quantitative comparisons between the three cases suggest that the shortcoming

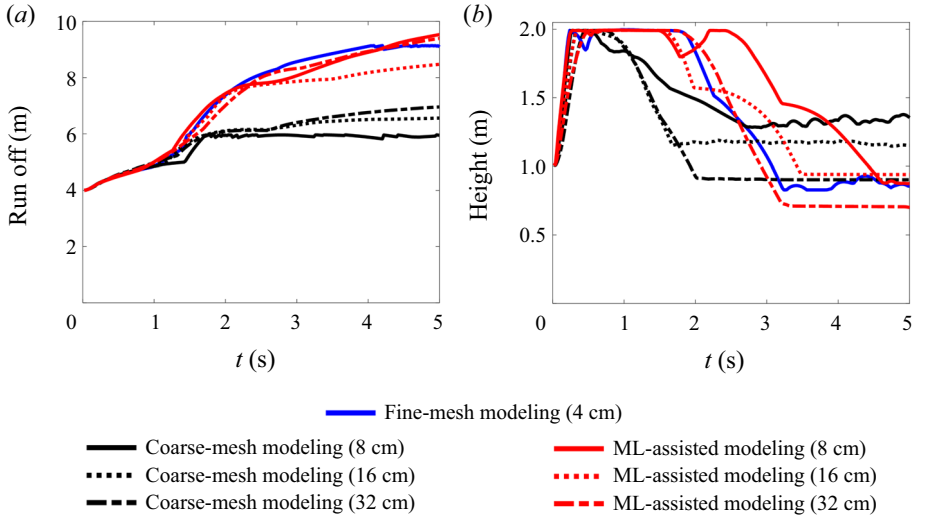

Figure 14. Runoff (*a*) and height (*b*) evolution of the granular system for fine-scale, coarse-scale and ML-assisted cases.

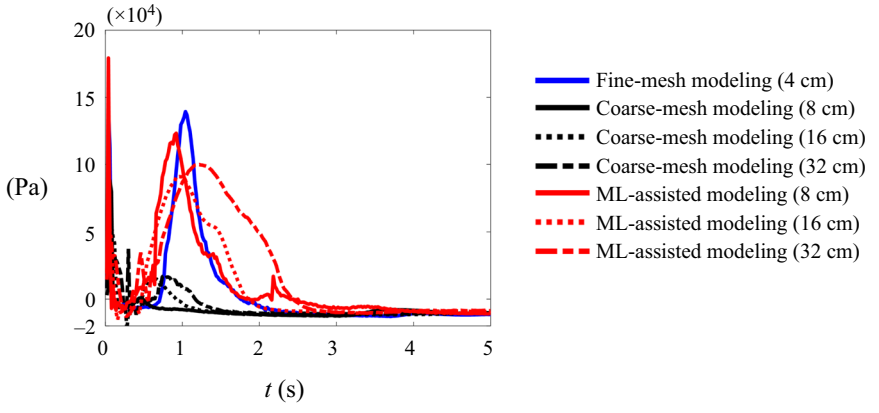

Figure 15. Evolution of average pressure of the fluid phase for fine-scale, coarse-scale and ML-assisted cases.

of coarse-scale modelling has for the most part been largely improved by combining it with a ML model previously trained on ground truth fine-scale data.

5. Conclusions

The importance of studying fluid–solid interactions is manifested in a large number of areas of science and engineering. It is, therefore, very important to have fast and accurate models that allow the modelling of these phenomena. Several computational techniques are used for simulating fluid–particle interactions, among which the coupling of CFD and DEM has proven to be most convenient in terms of computational costs, accuracies of predictions and complexity of implementation. However, the most prominent limitation of this approach is that it is largely dependent on the size of the mesh of the fluid domain.

The fact is, when the coupling is conducted on a large-scale mesh, even though it results in faster simulations, the results are inaccurate, and the fine-scale features are

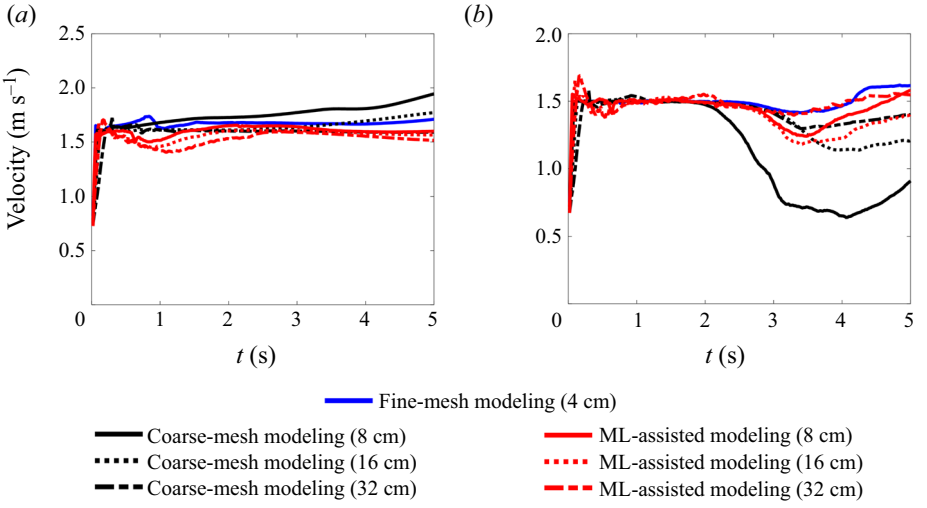

Figure 16. Evolution of velocity of the fluid phase for fine-scale, coarse-scale and ML-assisted cases; (*a*) average, (*b*) median.

not reproduced. On the other hand, when such modelling is used with a small-scale mesh, even though it results in significantly more accurate results, the computational time becomes prohibitive. One widely used approach to increase the size of the mesh while still retaining the accuracy of the modelling is to conduct a mesh-independence analysis, where scientists and engineers determine how much they can increase the size of the mesh and still obtain results that are still acceptably accurate. This method, however, usually results only in minor improvements in computational speeds. Therefore, it is still a challenge in the scientific community to find a way to be able to have both accurate and fast modelling using larger meshes.

In this paper, we proposed a coupled and assisted ML approach, where one of the major forces responsible for fluid–solid coupling is replaced with a ML model, which was previously trained on a ground truth fine-scale simulation. This framework ultimately allows more accurate modelling, while still using a coarse mesh. To test the capabilities of the new method, we conducted seven simulations, where the first case was fine-scale modelling (ground truth), the second, third and fourth were coarse-scale simulations (considerably less accurate, with mesh sizes of 8, 16 and 32 cm, respectively) and the final three cases were coarse-scale ML-assisted modelling on the same mesh sizes. The results of this research have demonstrated large improvements in 9 metrics, the most significant of which are run-off distance and height of the granular system, fine-scale features and the computation speedup. However, it should be noted that the effectiveness of this method was considerably diminished when used with a 32 cm mesh. One possible avenue for future research might be to reduce the computational cost using pruning operations of the ML model (Fukami *et al.* 2021; Mitra *et al.* 2021).

Acknowledgements. We would like to thank the anonymous reviewers who provided constructive comments on the earlier draft of the manuscript.

Funding. This study was partially supported by NSF (Grant no. CMMI-2000966) (*Fluid Dynamics*), NIH (Grant no. P20GM103432) and NASA (Grant no. 80NSSC19M0061).

Declaration of interests. The authors report no conflict of interest.

Author ORCIDs.
Pejman Tahmasebi http://orcid.org/0000-0001-5548-4805.

References

Aghaei Jouybari, M., Yuan, J., Brereton, G.J. & Murillo, M.S. 2021 Data-driven prediction of the equivalent sand-grain height in rough-wall turbulent flows. *J. Fluid Mech.* **912**, A8.

Antony, S.J., Zhou, C.H. & Wang, X. 2006 An integrated mechanistic-neural network modelling for granular systems. *Appl. Math. Model.* **30**, 116–128.

Ariana, M.A., Vaferi, B. & Karimi, G. 2015 Prediction of thermal conductivity of alumina water-based nanofluids by artificial neural networks. *Powder Technol.* **278**, 1–10.

Benvenuti, L., Kloss, C. & Pirker, S. 2016 Identification of DEM simulation parameters by artificial neural networks and bulk experiments. *Powder Technol.* **291**, 456–465.

Bertuola, D., Volpato, S., Canu, P. & Santomaso, A.C. 2016 Prediction of segregation in funnel and mass flow discharge. *Chem. Engng Sci* **150**, 16–25.

Brenner, M.P., Eldredge, J.D. & Freund, J.B. 2019 Perspective on machine learning for advancing fluid mechanics. *Phys. Rev. Fluids* **4**, 100501.

Brevis, I., Muga, I. & van der Zee, K.G. 2020 Data-driven finite elements methods: machine learning acceleration of goal-oriented computations. arXiv:2003.04485v1.

Brunton, S.L., Noack, B.R. & Koumoutsakos, P. 2020 Machine learning for fluid mechanics. *Annu. Rev. Fluid Mech.* **52**, 477–508.

Chaurasia, R.C. & Nikkam, S. 2017 Application of artificial neural network to study the performance of multi-gravity separator (MGS) treating iron ore fines. *Part. Sci. Technol.* **35**, 93–102.

Chen, F., Drumm, E.C. & Guiochon, G. 2011 Coupled discrete element and finite volume solution of two classical soil mechanics problems. *Comput. Geotech.* **38**, 638–647.

Chen, J., Orozovic, O., Williams, K., Meng, J. & Li, C. 2020 A coupled DEM-SPH model for moisture migration in unsaturated granular material under oscillation. *Intl J. Mech. Sci.* **169**, 105313.

Chen, W. & Qiu, T. 2012 Numerical simulations for large deformation of granular materials using smoothed particle hydrodynamics method. *Intl J. Geomech.* **12**, 127–135.

Chen, X., Zhong, W., Zhou, X., Jin, B. & Sun, B. 2012 CFD–DEM simulation of particle transport and deposition in pulmonary airway. *Powder Technol.* **228**, 309–318.

Crowe, C.T., Schwarzkopf, J.D., Sommerfeld, M. & Tsuji, Y. 2011 *Multiphase Flows with Droplets and Particles*. CRC Press.

Cui, Y., Chan, D. & Nouri, A. 2017 Discontinuum modeling of solid deformation pore-water diffusion coupling. *Intl J. Geomech.* **17**, 04017033.

Di Felice, R. 1994 The voidage function for fluid-particle interaction systems. *Intl J. Multiphase Flow* **20**, 153–159.

Ding, W.-T. & Xu, W.-J. 2018 Study on the multiphase fluid-solid interaction in granular materials based on an LBM-DEM coupled method. *Powder Technol.* **335**, 301–314.

Farizhandi, A.A.K., Zhao, H. & Lau, R. 2016 Modeling the change in particle size distribution in a gas-solid fluidized bed due to particle attrition using a hybrid artificial neural network-genetic algorithm approach. *Chem. Engng Sci.* **155**, 210–220.

Figueiredo, E., Moldovan, I., Santos, A., Campos, P. & Costa, J.C.W.A. 2019 Finite element–based machine-learning approach to detect damage in bridges under operational and environmental variations. *J. Bridge Engng.* **24**, 04019061.

Fukami, K., Fukagata, K. & Taira, K. 2019 Super-resolution reconstruction of turbulent flows with machine learning. *J. Fluid Mech.* **870**, 106–120.

Fukami, K., Fukagata, K. & Taira, K. 2020*a* Assessment of supervised machine learning methods for fluid flows. *Theor. Comput. Fluid Dyn.* **34**, 497–519.

Fukami, K., Fukagata, K. & Taira, K. 2020*b* Machine-learning-based spatio-temporal super resolution reconstruction of turbulent flows. *J. Fluid Mech.* **909**, A9.

Fukami, K., Hasegawa, K., Nakamura, T., Morimoto, M. & Fukagata, K. 2021 Model order reduction with neural networks: application to laminar and turbulent flows. *SN Comput. Sci.* **2**, 467.

Garbaa, H., Jackowska-Strumillo, L., Grudzien, K. & Romanowski, A. 2014 Neural network approach to ECT inverse problem solving for estimation of gravitational solids flow. In *2014 Federated Conference on Computer Science and Information Systems* (FedCSIS) vol. 34, pp. 19–26.

Gidaspow, D. 1994 *Multiphase Flow and Fluidization-Continuum and Kinetic Theory Descriptions*. Academic Press.

HAGER, A., KLOSS, C., PIRKER, S. & GONIVA, C. 2011 Parallel open source CFD-DEM for resolved particle-fluid interaction. In *9th International Conference on Computational Fluid Dynamics in the Minerals and Process Industries*. Melbourne.

HASSANPOUR, A., TAN, H., BAYLY, A., GOPALKRISHNAN, P., NG, B. & GHADIRI, M. 2011 Analysis of particle motion in a paddle mixer using discrete element method (DEM). *Powder Technol.* **206**, 189–194.

HERTZ, H. 1882 Ueber die Berührung fester elastischer Körper. *J. Für Die Reine Und Angew. Math. (Crelles Journal)* **1882**, 156–171.

HINCH, E.J. & SERAYSSOL, J.M. 1986 The elastohydrodynamic collision of two spheres. *J. Fluid Mech.* **163**, 479–497.

HÖHNER, D., WIRTZ, S. & SCHERER, V. 2013 Experimental and numerical investigation on the influence of particle shape and shape approximation on hopper discharge using the discrete element method. *Powder Technol.* **235**, 614–627.

HOULSBY, G.T.T. 2009 Potential particles: a method for modelling non-circular particles in DEM. *Comput. Geotech.* **36**, 953–959.

JAYASUNDARA, C.T., YANG, R.Y., GUO, B.Y., YU, A.B., GOVENDER, I., MAINZA, A., VAN DER WESTHUIZEN, A. & RUBENSTEIN, J. 2011 CFD–DEM modelling of particle flow in IsaMills – comparison between simulations and PEPT measurements. *Miner. Engng* **24**, 181–187.

JI, S., CHEN, X. & LIU, L. 2019 Coupled DEM-SPH method for interaction between dilated polyhedral particles and fluid. *Math. Probl. Engng* **2019**, 4987801.

JIANG, Y., KOLEHMAINEN, J., GU, Y., KEVREKIDIS, Y.G., OZEL, A. & SUNDARESAN, S. 2019 Neural-network-based filtered drag model for gas-particle flows. *Powder Technol.* **346**, 403–413.

KACHRIMANIS, K., KARAMYAN, V. & MALAMATARIS, S. 2003 Artificial neural networks (ANNs) and modeling of powder flow. *Intl J. Pharm.* **250**, 13–23.

KHAN, A.R. & RICHARDSON, J.R. 1989 Fluid-particle interactions and flow characteristics of fluidized beds and settling suspensions of spherical particles. *Chem. Engng Commun.* **78**, 111–130.

KIM, H., KIM, J., WON, S. & LEE, C. 2021 Unsupervised deep learning for super-resolution reconstruction of turbulence. *J. Fluid Mech.* **910**, A29.

KINGMA, D.P. & BA, J.L. 2015 Adam: A method for stochastic optimization. In *3rd International Conference on Learning Representations, ICLR 2015 - Conference Track Proceedings*. arXiv:1412.6980v9.

KOCH, D.L. & HILL, R.J. 2001 Inertial effects in suspension and porous-media flows. *Annu. Rev. Fluid Mech.* **33**, 619–647.

KU, X., LI, T. & LØVÅS, T. 2015 CFD–DEM simulation of biomass gasification with steam in a fluidized bed reactor. *Chem. Engng Sci.* **122**, 270–283.

KUTZ, J.N. 2017 Deep learning in fluid dynamics. *J. Fluid Mech.* **814**, 1–4.

LI, B., YANG, Z., ZHANG, X., HE, G., DENG, B.-Q. & SHEN, L. 2020*a* Using machine learning to detect the turbulent region in flow past a circular cylinder. *J. Fluid Mech.* **905**, A10.

LI, X., ZHAO, J. & KWAN, J.S.H. 2020*b* Assessing debris flow impact on flexible ring net barrier: a coupled CFD-DEM study. *Comput. Geotech.* **128**, 103850.

LIANG, L., LIU, M., MARTIN, C. & SUN, W. 2018*a* A deep learning approach to estimate stress distribution: a fast and accurate surrogate of finite-element analysis. *J. R. Soc. Interface* **15**, 20170844.

LIANG, L., LIU, M., MARTIN, C. & SUN, W. 2018*b* A machine learning approach as a surrogate of finite element analysis-based inverse method to estimate the zero-pressure geometry of human thoracic aorta. *Intl J. Numer. Meth. Biomed. Engng* **34**, e3103.

LIASHCHYNSKYI, P. & LIASHCHYNSKYI, P. 2019 Grid search, random search, genetic algorithm: a big comparison for NAS. arXiv:1912.06059v1.

LING, Y., WAGNER, J.L., BERESH, S.J., KEARNEY, S.P. & BALACHANDAR, S. 2012 Interaction of a planar shock wave with a dense particle curtain: modeling and experiments. *Phys. Fluids* **24**, 113301.

LU, L.-S. & HSIAU, S.-S. 2008 DEM simulation of particle mixing in a sheared granular flow. *Particuology* **6**, 445–454.

MAHDI, F.M. & HOLDICH, R.G. 2017 Using statistical and artificial neural networks to predict the permeability of loosely packed granular materials. *Sep. Sci. Technol.* **52**, 1–12.

MANDAL, S. & KHAKHAR, D.V. 2016 A study of the rheology of planar granular flow of dumbbells using discrete element method simulations. *Phys. Fluids* **28**, 103301.

MITRA, P., VENKATESAN, V., JANGID, N., NAMBIAR, A., KUMAR, D., ROA, V., SANTO, N.D., HAGHSHENAS, M., MITRA, S. & SCHMIDT, D. 2021 Network compression for machine-learnt fluid simulations. arXiv:2103.00754v1.

O'SULLIVAN, C. 2011 *Particulate Discrete Element Modelling*. Taylor & Francis.

PARK, J. & CHOI, H. 2020 Machine-learning-based feedback control for drag reduction in a turbulent channel flow. *J. Fluid Mech.* **904**, A24.

PAYNE, F.C., QUINNAN, J.A., POTTER, S.T. & PRESS, C.R.C. 2008 *Remediation Hydraulics*. CRC Press.
PRIETO, J.L. 2020 Viscoelastic effects on drop deformation using a machine learning-enhanced, finite element method. *Polymers (Basel)* **12**, 1652.
RADL, S. & SUNDARESAN, S. 2014 A drag model for filtered Euler-Lagrange simulations of clustered gas-particle suspensions. *Chem. Engng Sci.* **117**, 416–425.
RAMEZANI, M., SUN, B., SUBRAMANIAM, S. & OLSEN, M.G. 2018 Detailed experimental and numerical investigation of fluid–particle interactions of a fixed train of spherical particles inside a square duct. *Intl J. Multiphase Flow* **103**, 16–29.
RYCROFT, C.H., ORPE, A.V. & KUDROLLI, A. 2009 Physical test of a particle simulation model in a sheared granular system. *Phys. Rev.* E **80**, 031305.
SUZUKI, K., BARDET, J.P., ODA, M., IWASHITA, K., TSUJI, Y., TANAKA, T. & KAWAGUCHI, T. 2007 Simulation of upward seepage flow in a single column of spheres using discrete-element method with fluid-particle interaction. *J. Geotech. Geoenviron. Engng* **133**, 104–109.
TANG, Y., CHAN, D.H. & ZHU, D.Z. 2017 A coupled discrete element model for the simulation of soil and water flow through an orifice. *Intl J. Numer. Anal. Methods Geomech.* **41**, 1477–1493.
TONG, Z.B., ZHENG, B., YANG, R.Y., YU, A.B. & CHAN, H.K. 2013 CFD-DEM investigation of the dispersion mechanisms in commercial dry powder inhalers. *Powder Technol.* **240**, 19–24.
TOPIN, V., MONERIE, Y., PERALES, F. & RADJAÏ, F. 2012 Collapse dynamics and runout of dense granular materials in a fluid. *Phys. Rev. Lett.* **109**, 188001.
TSUJI, Y., KAWAGUCHI, T. & TANAKA, T. 1993 Discrete particle simulation of two-dimensional fluidized bed. *Powder Technol.* **77**, 79–87.
VIDYAPATI, V. & SUBRAMANIAM, S. 2013 Granular flow in silo discharge: discrete element method simulations and model assessment. *Ind. Engng Chem. Res.* **52**, 13171–13182.
WAGNER, J.J., SHU, H., KILAMBI, R. & HIGGS, C.F. 2019 Experimental investigation of fluid-particle interaction in binder jet 3D printing. In *Proceedings of the 30th Annual International Solid Freeform Fabrication Symposium - An Additive Manufacturing Conference SFF* 2019, pp. 134–147. Preprints.
WAN, Z.Y. & SAPSIS, T.P. 2018 Machine learning the kinematics of spherical particles in fluid flows. *J. Fluid Mech.* **857**, R2.
WAN, J., WANG, F., YANG, G., ZHANG, S., WANG, M., LIN, P. & YANG, L. 2018 The influence of orifice shape on the flow rate: a DEM and experimental research in 3D hopper granular flows. *Powder Technol.* **335**, 147–155.
WU, C., CHENG, Y., DING, Y. & JIN, Y. 2010 CFD–DEM simulation of gas–solid reacting flows in fluid catalytic cracking (FCC) process. *Chem. Engng Sci.* **65**, 542–549.
XU, W.J., DONG, X.Y. & DING, W.T. 2019 Analysis of fluid-particle interaction in granular materials using coupled SPH-DEM method. *Powder Technol.* **353**, 459–472.
XU, B.H., FENG, Y.Q., YU, A.B., CHEW, S.J. & ZULLI, P. 2001 A numerical and experimental study of the gas-solid flow in a fluid bed reactor. *Powder Handl. Process.* **13**, 71–76.
XU, W.-J., HU, L.-M. & GAO, W. 2016 Random generation of the meso-structure of a soil-rock mixture and its application in the study of the mechanical behavior in a landslide dam. *Intl J. Rock Mech. Min. Sci.* **86**, 166–178.
XU, B.H. & YU, A.B. 1997 Numerical simulation of the gas-solid flow in a fluidized bed by combining discrete particle method with computational fluid dynamics. *Chem. Engng Sci.* **52**, 2785–2809.
YANG, G.C., JING, L., KWOK, C.Y. & SOBRAL, Y.D. 2019 A comprehensive parametric study of LBM-DEM for immersed granular flows. *Comput. Geotech.* **114**, 103100.
ZHANG, Y., JIA, F., ZENG, Y., HAN, Y. & XIAO, Y. 2018*a* DEM study in the critical height of flow mechanism transition in a conical silo. *Powder Technol.* **331**, 98–106.
ZHANG, X. & TAHMASEBI, P. 2019 Effects of grain size on deformation in porous media. *Transp. Porous Media* **129**, 321–341.
ZHANG, Z., ZHANG, X., QIU, H. & DADDOW, M. 2016 Dynamic characteristics of track-ballast-silty clay with irregular vibration levels generated by high-speed train based on DEM. *Constr. Build. Mater.* **125**, 564–573.
ZHANG, Z.-H., ZHANG, X., TANG, Y. & CUI, Y. 2018*b* Discrete element analysis of a cross-river tunnel under random vibration levels induced by trains operating during the flood season. *J. Zhejiang Univ.* A **19**, 346–366.
ZHAO, J. & SHAN, T. 2013*a* Coupled CFD-DEM simulation of fluid-particle interaction in geomechanics. *Powder Technol.* **239**, 248–258.
ZHAO, J. & SHAN, T. 2013*b* Numerical modeling of fluid-particle interaction in granular media. *Theor. Appl. Mech. Lett.* **3**, 021007.

ZHU, H.P., ZHOU, Z.Y., YANG, R.Y. & YU, A.B. 2007 Discrete particle simulation of particulate systems: theoretical developments. *Chem. Engng Sci.* **62**, 3378–3396.

ZHU, H.P., ZHOU, Z.Y., YANG, R.Y. & YU, A.B. 2008 Discrete particle simulation of particulate systems: a review of major applications and findings. *Chem. Engng Sci.* **63**, 5728–5770.